Photothermal optical coherence microscopy for studying lipid architecture in human carotid arteries

Deen, Aaron Doug; Lopez-Marin, Antonio; Riksen, Jonas J.M.; Van Der Steen, Antonius F.W.; Van Soest, Gijs

DOI
10.1364/BOE.534800

Publication date
2024

Document Version
Final published version

Published in
Biomedical Optics Express

Research Article Vol. 15, No. 12 / 1 Dec 2024 / Biomedical Optics Express 6654
Biomedical Optics EXPRESS

Photothermal optical coherence microscopy for studying lipid architecture in human carotid arteries

AARON DOUG DEEN,[1] ANTONIO LÓPEZ-MARÍN,[1] JONAS J. M. RIKSEN,[1] ANTONIUS F. W. VAN DER STEEN,[1,2,3] AND GIJS VAN SOEST[1,3,4,*]

[1]Department of Cardiology, Cardiovascular Institute, Thorax Center, Erasmus MC, The Netherlands
[2]Department of Imaging Science and Technology, Delft University of Technology, The Netherlands
[3]Department of Precision and Microsystems Engineering, Delft University of Technology, The Netherlands
[4]Wellman Center for Photomedicine, Massachusetts General Hospital, Boston, USA
*g.vansoest@erasmusmc.nl

Abstract: Photothermal optical coherence microscopy (PT-OCM) combines the high-resolution, label-free morphological imaging of OCM with the ability to discriminate tissue composition through phase-sensitive photothermal imaging. In this study, we perform 2D imaging of human carotid endarterectomies to spectrally determine lipid distribution, with verification via histologically stained samples. The structural information from OCM is combined with the spectral information gained from measuring the resulting sample surface displacement from thermoelastic expansion, following light irradiation. PT-OCM is thus demonstrated as a potential tool in the investigation of atherosclerotic plaque lipids, contributing towards the understanding of plaque instability.

1. Introduction

The ability to differentiate tissue composition and structure in a noninvasive, label-free form has been highly desired yet challenging to achieve, due to a trade-off between structural detail and molecular contrast. Optical coherence tomography (OCT) has the ability to produce rapid volumetric imaging of tissue microstructure through measurements of sample backscattered light [1]. These properties have established OCT as an indispensable tool in medicine by offering non-invasive, high-resolution imaging of tissue morphology without the need for tissue staining or contact. Its microscopic derivative, named optical coherence microscopy (OCM), trades imaging depth for micron-level, in-plane resolution, enabling detailed visualization of cellular and subcellular structures [2,3]. OCM has had widespread applications ranging from depth-resolved imaging of the retinal layers to identification of plaque characteristics [4–10]. However, though OCT and OCM provide high-resolution tissue morphology, they lack chemically specific tissue contrast.

To overcome the main limitation of conventional OCM, various functional extensions have been proposed to provide molecular contrast. Spectroscopic OCT (SOCT) extracts the spectral content of the tissue within the bandwidth of the OCT laser source offering biochemical information [11–14]. By utilizing the phase signal of OCT, optical coherence elastography (OCE) may quantify the biomechanical properties of biological tissue finding applications in detecting cancer and fibrotic diseases [15–17]. Phase information can further be used to provide quantitative measurements of blood flow and velocity extracted from the Doppler frequency shift through Doppler OCT (DOCT) [18–20]. As a final example, polarization-sensitive OCT (PS-OCT) measures changes in the polarization state of light through tissue birefringence, contributing significantly to the fields of ophthalmology and dermatology [21–23].

#534800 https://doi.org/10.1364/BOE.534800
Journal © 2024 Received 8 Jul 2024; revised 27 Aug 2024; accepted 27 Aug 2024; published 4 Nov 2024

Biomedical Optics EXPRESS

Photothermal OCT (PT-OCT) and its less common microscopic implementation (PT-OCM) are functional extensions of OCT that offer optical absorption contrast combined with OCT's high-resolution morphology. PT-OCT utilizes the photothermal effect in which a modulated laser source is used to induce a localized temperature rise in biological tissue. The increase in local temperature leads to a thermal expansion of the tissue, as well as a change in refractive index [24]. The combined effect, with thermoelastic expansion as the dominant contributor, is a change in the optical path length of the backscattered light. This is then detected as a change in phase in the OCT signal. Thus, optical absorption contrast is achieved through the intrinsic light absorption by endogenous chromophores, by choosing salient excitation wavelengths. Applications of PT-OCT have ranged from the use of gold nanorods as contrast agents for molecular imaging, to single-cell imaging [25–28]. However, major limitations of traditional PT-OCT were its use of continuous wave lasers for modulation which led to heating of the tissue samples coupled with long measurement times. Recent advances in modulated PT-OCT have somewhat alleviated these limitations by reducing frame acquisition time to the order of hundreds of microseconds [29,30].

In previous work, we applied a nanosecond pulsed laser to overcome the limitations of heating and acquisition time by conventional PT-OCT. We further demonstrated its viability in improving the acquisition speed of PT-OCT to the single-microsecond range, offering the potential for spectroscopic imaging [31]. We now advance to the cellular regime with PT-OCM, demonstrating its ability to map lipid distribution on human carotid endarterectomy (CEA) samples via high spatial resolution spectroscopy. This is all coupled with 2D imaging with overlayed surface displacement maps on OCM's high-resolution morphology.

2. Materials and methods

2.1. Phase-sensitive OCT interferometer with the FDML laser

For interrogation, a phase-sensitive OCT (PhS-OCT) system built upon a dispersion-compensated, 1.6 MHz Fourier-domain mode-locked laser (FDML) is utilized [33]. Figure 1 illustrates the schematic layout of the FDML laser resonator, which is equipped with a 4x buffer stage. In short, a high-speed laser diode driver is used to modulate the semiconductor optical amplifier (SOA), achieving a laser duty cycle of 25%. Following this, the laser's full wavelength sweep range of 108 nm around a central wavelength of 1316 nm is delayed and time-interleaved with copies of the original sweep in the subsequent 4x buffer stage. This results in an effective duty cycle of 100% at a sweep rate of 1.6 MHz. The output generated from the FDML laser is divided in a 9:1 ratio, where 90% of the output power is directed to the sample arm, while the remaining 10% is sent to the reference arm. The reflected light from the sample arm is recombined with the light from the reference arm in a 50/50 coupler. The laser achieves an output power of 3 mW on the sample with a sensitivity of 102 dB and a phase stability of 0.5 nm in air. The coherence fringes were captured by a 1.6 GHz, InGaAs balanced photodetector (PDB480C-AC, Thorlabs, NJ, US), and subsequently transformed into a digital signal through a 4 GS/s, 8-bit data acquisition card (CobraMax, Gage, IL, US).

2.2. Photothermal optical coherence microscopy

For interrogation, the OCT beam was collimated with a 1310 nm air-spaced doublet (F810APC-1310, Thorlabs, NJ, US), expanded to fill the entrance pupil of the objective with a plano-concave lens (LC1582-C-ML, Thorlabs, U.S.), then collimated with a spherical singlet (LBF254-150-C, Thorlabs, U.S.). The collimated beam is then reflected off a 50:50 UVFS beamsplitter (BSW30, Thorlabs, U.S.) onto a mirror (PF10-03-P01, Thorlabs, U.S.) and directed into an infinity-corrected objective lens (PAL-20-NIR-HR-LC00, Mitutoyo, Japan), focusing the light on the sample.

To induce thermoelastic deformation, we integrated a wavelength tunable pulsed optical parametric oscillator (OPO) laser (SpitLight EVO-OPO, Innolas, Germany) into the PhS-OCT

Biomedical Optics EXPRESS

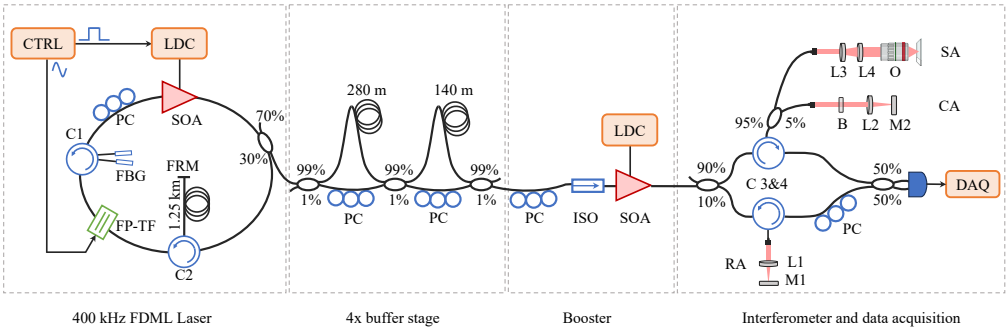

Fig. 1. Schematic of the FDML Swept-Source OCT system. (a) Schematic of the setup based on a wavelength tunable pulsed laser and a 1.6 MHz phase-sensitive OCT system. CTRL, driver and control electronics, LDC, laser diode controller, PC, polarization controller, SOA, semiconductor optical amplifier, FBG, fiber Bragg grating, FP-TF, Fabry-Pérot tunable filter, FRM, Faraday rotation mirror, C1-4, circulators 1-4, ISO, isolator, RA, reference arm, L1-4, lenses 1-4, M1-2, mirrors 1-2, B, calibration block, SA, sample arm, CA, calibration arm, OCT, optical coherence tomography, FDML, Fourier domain mode-locked, DAQ, data acquisition card. [Adapted] with permission from [32] © The Optical Society.

system as shown in Fig. 2(a). The pulsed laser has a wavelength tuning range of 660 - 2400 nm with pulse durations of 4 - 7 ns and repetition rates of 10 - 200 Hz. Output light from the pulsed laser was attenuated to desired levels using absorptive neutral density filters then directed by two protected silver mirrors (PF10-03-P01, Thorlabs, U.S.) onto a plano-convex lens for collimation (LA5012, Thorlabs, U.S.). The collimated beam is then spatially filtered by focusing the beam with a best-form lens (LBF254-40, Thorlabs, U.S.) through a high-power aperture (200 µm Copper Aperture #39-894, Edmund Optics, U.S.) then recollimated with a second, best-form lens (LBF254-075, Thorlabs, U.S.). The beam size is then reduced and collimated with a lens pair (LBF254-050, LC1715-ML, Thorlabs, U.S.) traveling through a beam sampler (BSF10-C, Thorlabs, U.S.), beamsplitter and reflected off a mirror into the objective and focused on the sample. The light from the beam sampler is directed towards a nanosecond InGaAs photodetector (1623, Newport, U.S.) recording shot-to-shot fluctuations in the pulsed laser energy. This is later used in postprocessing for power compensation. Note that no dichroic mirrors or beamsplitters were used in the system, so spectral overlap exists between the OCT beam and pulsed laser beam across the spectral band of the OCT wavelength sweep range (1262–1370 nm). However, the effect is negligible as there is no temporal overlap between the beams allowing clear separation of the two.

The spot sizes of the co-aligned beams were measured by imaging a negative 1951 USAF test target (R3L3S1N, Thorlabs, U.S.), then fitting the edge-spread function (ESF) acquired by scanning across an edge of the test target (Fig. 2(b), c). The line-spread function (LSF) was then calculated by taking the derivative of the ESF. The lateral resolution of the probe beam, measured as the full width at half-maximum (FWHM) of the LSF, is diffraction limited at approximately 1.4 µm as seen in Fig. 2(d) while the excitation beam has a FWHM of 14 µm and is kept larger than the probe beam following the thermoelastic model [31]. Images of the biological samples were generated by raster scanning a 3-axis translational stage setup (X-LDM110C-AE54D12, Zaber, Canada; KMTS50E/M, Thorlabs, U.S.; LTA-HS, Newport, U.S.).

2.3. Hardware synchronization

A digital delay generator with a 100 MHz internal clock was employed in a master-slave configuration to synchronize the movement of the stages, OCT data acquisition, photodiode

Biomedical Optics EXPRESS

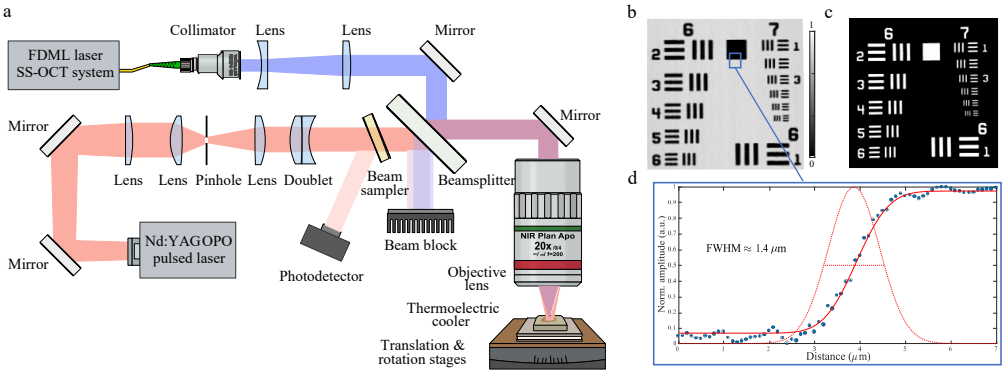

Fig. 2. Photothermal optical coherence microscopy imaging system. (a) Schematic of the setup consisting of a 1.6 MHz Fourier domain mode-locked swept-source OCT system (see Fig. 1) coupled with a nanosecond pulsed wavelength tunable laser. (b) Acquired 2D image of a USAF target. (c) Stock photo of a USAF resolution target [33]. (d) Lateral resolution derived from the edge spread function obtained by scanning a line across the resolution target. A lateral resolution of 1.4 μm FWHM is achieved.

detection and pulse emission from the pulsed laser, as seen in Fig. 3. A square wave with a duty cycle equal to an entire line (B-scan) was generated by channel A for control of the XY stages for raster scanning. The fast-axis linear stage moves while the signal is high then returns to its original position when the signal is low, with movement of the slow-axis stage occurring simultaneously. The output of Channel B is passed through an arbitrary waveform generator and converted to a sine wave at the same frequency. Since the FDML laser is untriggered and free running at 390 kHz, a high-speed comparator is employed to produce an output pulse, aligning the master A-line of the FDML laser with the output of Channel B. The output of the comparator is sent to a 4 GS/s data acquisition card for acquisition of sample data from the balanced photodetector. Channels C and D are dedicated to the control of the diode pump and Pockels cell of the pulsed laser, respectively. Two pulse trains at the same frequency are generated in which the Pockels cell trigger is delayed by n μs to the diode pump to control the excitation energy of the Q-switched laser. Finally, Channel E is used to trigger the acquisition of a second data acquisition card which stores the output of an external photodetector for power compensation. Note that with the exclusion of the trigger for the XY stages and the FDML clock, all other signals are operated at the same frequency, simply with varying delays.

2.4. *Processing pipeline*

The processing pipeline from raw data to the final image is depicted in Fig. 4. For background compensation 100 A-lines were acquired and averaged with the reference and sample arms alternately opened and closed. 100 A-lines are then acquired off the reference mirror and background compensation applied. Moving average and bandpass filters were then applied to the average of the A-lines to compensate for any residual noise following background compensation. The Hilbert Transform is then applied to obtain the unwrapped phase, and the polynomial coefficients extracted for later use in resampling the acquired sample data in K-linearization. For imaging, sample data of a specimen of interest is acquired from the sample arm and background compensation applied. This is followed by windowing to reduce phase noise, then the resampling of the acquired data (K-linearization) using the previously calculated coefficients. This is performed to compensate for the non-linear frequency sweep of the swept-source laser. Numerical dispersion compensation is then applied in the frequency domain to correct for dispersion effects. The inverse Fourier Transform is then performed providing a complex dataset.

Biomedical Optics EXPRESS

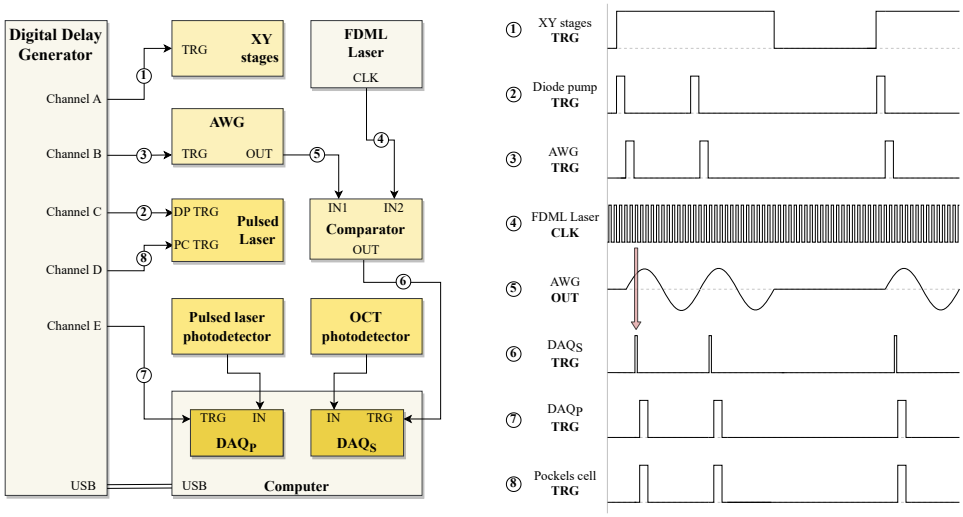

Fig. 3. Timing diagram for hardware synchronization. TRG, trigger, FDML, Fourier domain mode-locked, CLK, clock, AWG, arbitrary waveform generator, DP, diode pump, PC, Pockels cell, DAQ_P, data acquisition power compensation, DAQ_S, data acquisition OCT sample arm.

The magnitude of this dataset is taken to create the reflectance image, while the phase angle is calculated from the complex data. For each M-scan consisting of 16 A-lines acquired at the same location, 4 A-lines prior to the arrival of the laser pulse are subtracted from 4 A-lines following the pulse to obtain the change in displacement following laser irradiation. The resulting 4 A-lines are then averaged, and power compensation is applied using the pulse data from an external diode. Additional compensation for the optical components is performed for the beamsplitter, NIR filters and objective for differences in transmission across their active wavelength range. Finally, the phase value is assigned to the corresponding pixel location in the 2D image and overlayed on the 2D reflectance image. All processing was implemented in MATLAB.

2.5. System characterization for spectral acquisition

The phase noise floor of the system was determined by measuring the fluctuation in phase across the surface of a glass slide. Figure 5 shows the average of 1000 M-scans consisting of 16 A-lines per M-scan with a mean displacement of 0.4 nm (blue line), a standard deviation of approx. 0.5 nm and a min-max range of approx. 3.7 nm. Note that in an M-scan, a phase change is computed by subtracting A-lines in groups of 4 from the initial 4 A-lines. Thus, the first 4 A-lines have a resulting value of 0 and are discarded.

2.6. Imaging protocol

2.6.1. Spectra of pure lipids

To evaluate the spectroscopic capabilities of the system, spectra were acquired on three pure lipids: cholesteryl, cholesteryl linoleate, and cholesteryl oleate, as illustrated in Fig. 6. The pure lipids were dissolved from powder form in 1 mL HPLC-grade chloroform then deposited onto a glass slide. The chloroform was left to evaporate leaving the lipid deposit on the slide. In the spectral acquisition of the esters, the pulsed laser was wavelength scanned across the range of 1150 - 2000nm, in 1 nm increments with 20 pulses averaged per wavelength. The sweep was performed at a repetition rate of 100 Hz with pulse energies ranging from 750 nJ at 1150 nm to

Biomedical Optics EXPRESS

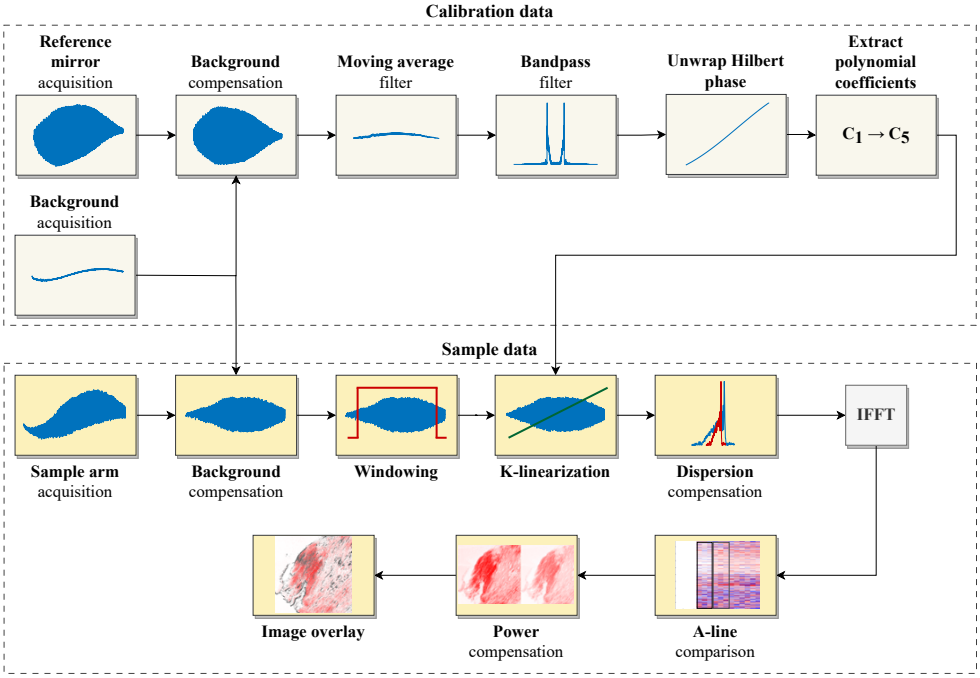

Fig. 4. Processing pipeline for PT-OCM acquisition from raw data to reflectance and phase images.

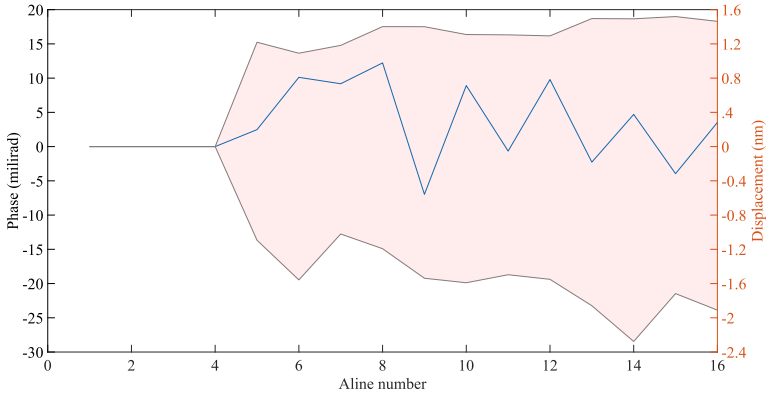

Fig. 5. Phase noise floor of PT-OCM system with mean and standard deviation.

130 nJ at 2000nm. These fluctuations were compensated for in postprocessing by monitoring the pulse energy with an external photodetector.

2.6.2. Large area mapping

PT-OCM imaging was performed on a human CEA specimen, first, with a large area image of the entire cross-section to determine two regions of interest (ROIs) based on their morphological and apparent lipid distribution within a 1 mm^2 area. The entire sample was raster scanned, encompassing 9 mm^2 (600×600 pixels) with a 14 µm step size, resulting in a 65 min scan time. To locate lipid-rich areas offering sufficient optical absorption contrast, optical excitation at 1720nm (100 Hz) was employed with a pulse energy of approximately 2 µJ per pulse.

Biomedical Optics EXPRESS

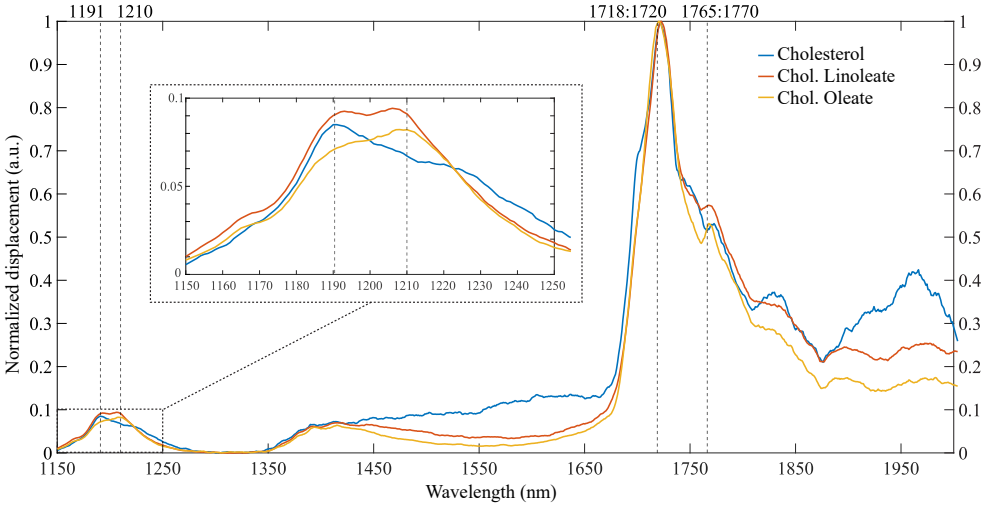

Fig. 6. PT-OCM spectra of 3 pure lipids. Normalized spectra of cholesterol, cholesterol linoleate and cholesterol oleate across the wavelength range 1150-2000nm with the 1150-1250 nm spectral region magnified.

2.6.3. Full-resolution imaging of regions of interest

High-resolution imaging was performed on two 1 mm^2 (720 × 720 pixels) ROIs. A step size of 1.4 µm was used, matching the diffraction-limited OCM spot size resulting in a scan time of 92 minutes. The area was raster scanned using two excitation wavelengths alternatingly, 1580 nm to highlight water absorption and 1720nm for lipid absorption, with the pulsed laser operated at a 100 Hz repetition rate. Absorptive neutral density filters were employed to equalize the excitation energy to approximately 2 µJ per pulse for both wavelengths. Following acquisition, the surface displacement at 1580 nm was subtracted from that at 1720nm to produce a water-compensated image.

2.6.4. Spectroscopic analysis of regions of interest

Morphological features and lipid absorption observed in the water-compensated images led to the selection of four regions for spectral analysis. Each selected region was subdivided into three sub-regions, spaced 14 µm apart, aligning with the pulsed laser spot size. In each sub-region, six spectra were acquired, for a total of 18 spectra for each designated area. These spectra were categorized into two sets: one set comprised three spectra spanning the wavelength range of 1100 to 1300 nm, and the other set consisting three spectra covering 1650 to 1800nm, both acquired in 1 nm wavelength steps and averaging 20 pulses per wavelength. For the 1100 - 1300 nm spectra, pulse energies ranged from 8.8 µJ at 1100 nm to 6.6 µJ at 1300 nm. A lower pulse energy was utilized for the 1650–1800nm range (2.3 µJ – 1.5 µJ) due to a 7-fold increase in optical absorption by lipids near the 1700nm band. For all spectra the pulsed laser was operated at 100 Hz resulting in a spectral acquisition time of 70 s for both wavelength ranges. Finally, for each area encompassing 18 spectra, averages were computed and compared to other areas for their respective wavelength ranges.

2.6.5. Tissue collection and processing

Human carotid endarterectomy specimens were surgically obtained, snap-frozen, and then stored at −80°C for subsequent examination. The tissue collection adhered to the ethical guidelines set by the Erasmus MC Ethics Board, as outlined in protocol MEC 2008-147. This surgical method

Biomedical Optics EXPRESS

maintains the structural integrity of the plaque and the lumen. Each CEA specimen was cut transversely into 3 mm thick blocks then embedded in 10% type A porcine gelatin (Sigma-Aldrich, Netherlands). To facilitate imaging, each block was cryo-sectioned into triplets (one 30 µm thick section for PT-OCM imaging and two adjacent 10 µm thick sections for histology) and mounted on glass slides. Histology was subsequently performed using Oil Red O (ORO) staining to highlight lipids and Hematoxylin–Eosin (H&E) staining for tissue morphology. For imaging, tissue sections were thawed and imaged as fresh tissue, at a fixed temperature of 10 °C without any fixation method applied to the samples.

3. Results

The spectra acquired from the pure lipid samples are shown in Fig. 6 and were normalized with peak surface displacements occurring in the 1718–1720nm range. Additionally, a second absorption band is present in the 1765-1770nm range. The 1150–1250 nm range, absorption peaks are highlighted in the zoomed area showing a left-shifted peak for cholesterol, a right-shifted peak for cholesteryl oleate and balanced absorption for cholesteryl linoleate.

The vessel's morphological details are depicted in the OCM intensity image in Fig. 7(a) and compared to the histologically stained Hematoxylin–Eosin (H&E) section depicted in Fig. 7(b) for morphological comparison. The corresponding surface displacement derived from the phase change is depicted in Fig. 7(c), specifically highlighting the presence of lipids and compared to an Oil Red O (ORO) stained section (Fig. 7(d)) for validation of lipid distribution. It is worth noting that the PT-OCM dataset inherently contains both intensity and phase information, acquired simultaneously, ensuring that the respective images are co-registered.

To investigate lipid distribution within human carotid arteries, we acquired two 2D images of 1 mm^2 each, at full resolution, employing a step size of 1.4 µm. In the first region of interest (ROI; labelled 1 in Fig. 7), the traditional OCM intensity image shows the microstructure of the vessel corresponding to structures observed in the H&E histology, as seen in Figs. 8(a) and 8(b), respectively. However, insights into the composition of the tissue cannot be derived solely from the intensity image. Figures 8(c) and 8(d) illustrate the surface displacement resulting from irradiating the artery with wavelengths of 1580 nm and 1720nm. We selected 1580 nm as a background control owing to its substantial water absorption (~8.0 cm^{-1}) and low lipid absorption (~0.2 cm^{-1}) characteristics [34]. A predominantly uniform surface displacement was observed across the vessel which was attributed to water absorption. To delineate the 'true' lipid distribution, we subtracted the surface displacement image obtained at 1580 nm from that at 1720nm, resulting in a water-compensated surface displacement image as depicted in Fig. 8(e). Lipid-rich regions in the water-compensated image are highlighted in deep red, indicating high surface displacement, which correspond to similarly marked lipid-rich areas observed in the Oil Red O (ORO) histology, seen in Fig. 8(f).

Morphological features and lipid absorption observed in the water-compensated images led to the selection of four regions for spectral analysis (see Methods for details), denoted as groups 1-4 in Fig. 9(a), with their respective locations highlighted in the ORO image. For each area encompassing 18 spectra, averages were computed and results for the 1100–1300 nm range were plotted in Fig. 9(b), with the 1650–1800nm range illustrated in Fig. 9(c). A discernible shift in peak absorption is observed in Fig. 9(b), where region 1 exhibits a peak absorption at 1209 nm and region 4 at 1189 nm. Regions 2 and 3 display spectra that contain a combination of the absorption peaks at 1189 and 1209 nm. The 1650–1800nm range in Fig. 9(c) shows peak absorptions at approximately 1718nm for groups 1 and 2, while regions 3 and 4 have peaks closer to 1726nm. Notably, an absorption peak around 1767nm indicates the potential presence of an additional lipid species' absorption band [35].

Full-resolution PT-OCM images were acquired in ROI 2 employing the same dual-wavelength imaging at 1580 nm and 1720nm. The OCM intensity image, presented in Fig. 10(a), reveals

Biomedical Optics EXPRESS

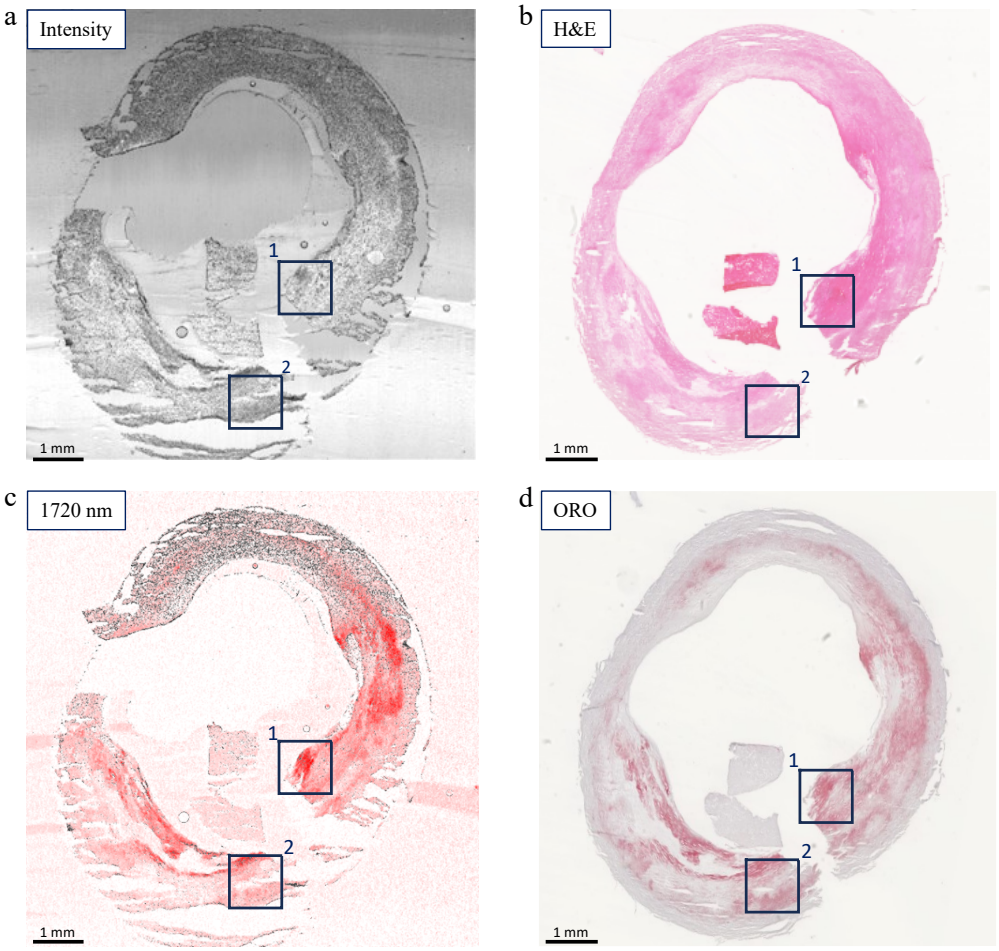

Fig. 7. Large area low-resolution map of a carotid endarterectomy specimen compared to histology. (a) Intensity OCM image of carotid artery cross-section. (b) H&E-stained histology of carotid artery. (c) Surface displacement overlayed on intensity image of carotid excited at 1720nm. (d) ORO-stained section of carotid artery. Boxes labeled 1 and 2 indicate areas in which high-resolution scans were acquired.

the microstructural details of the carotid artery, which align closely with those observed in the H&E histology (Fig. 10(b)). Notably, a qualitative distinction is evident in this region; the tissue proximal to the lumen, depicted in the top half of the figure, exhibits a denser composition compared to the tissue at the bottom, which is also observed in the H&E histology. The surface displacement images, shown in Figs. 10(c) and 10(d) for 1580 nm and 1720nm respectively, show consistent trends with those identified in ROI 1. At 1580 nm, surface displacement appears uniformly across the vessel. Conversely, at 1720nm, a variation in lipid structure and intensity is discernible, with concentrated lipid deposits near the vessel's lumen observed as high surface displacement, and diminishing concentration observed with increasing distance from the lumen. The difference is clearer in Fig. 10(e) when it is compared to the ORO histology in Fig. 10(f).

Continuing our analysis, four areas were selected based on their proximity to the vessel lumen, guided by the same morphological and lipid criteria previously described. These areas are illustrated in Fig. 11(a), with their specific locations emphasized in the corresponding ORO histology. A notable shift in peak absorption is observed in Fig. 11(b). Specifically, region 1

Biomedical Optics EXPRESS

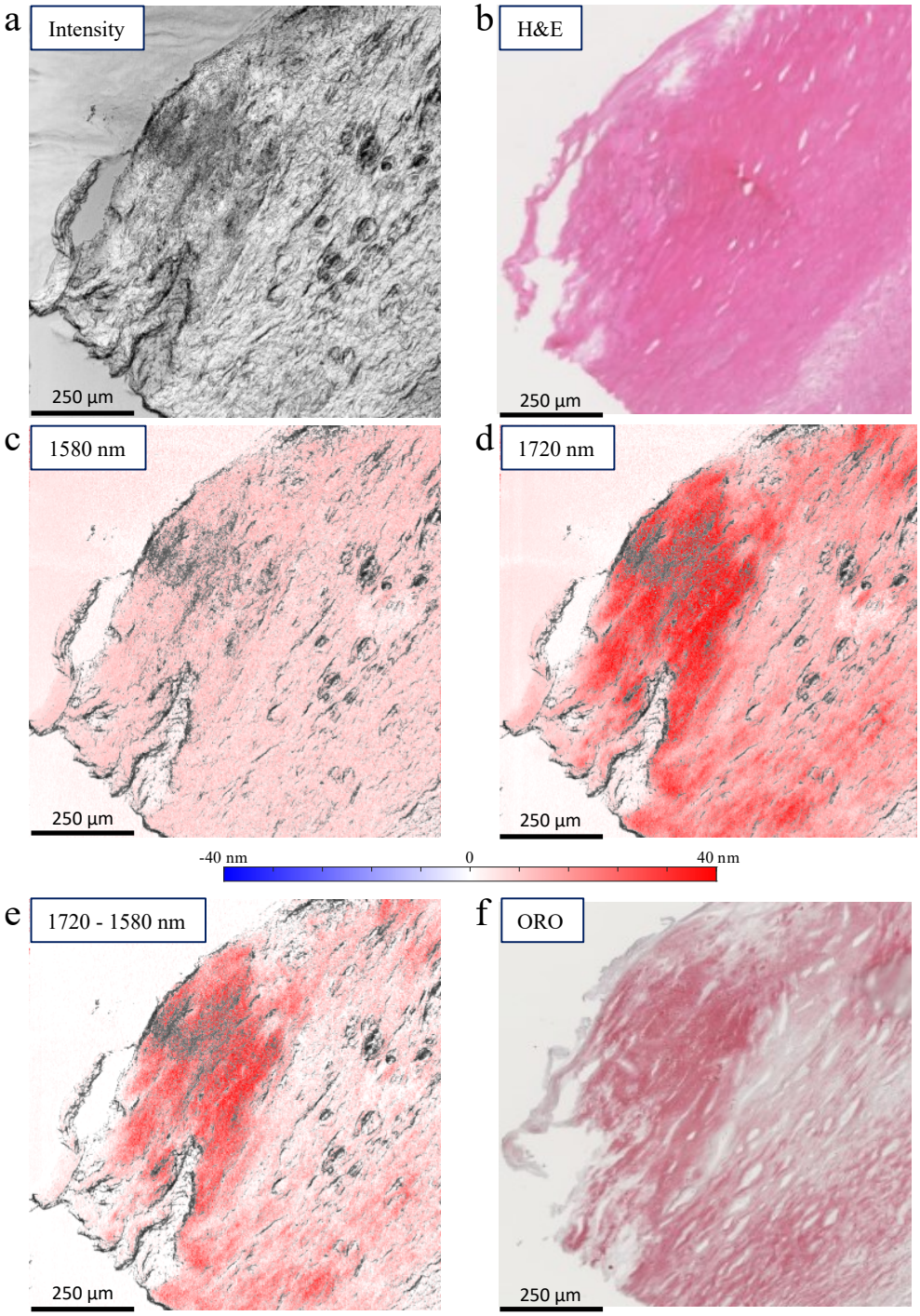

Fig. 8. High-resolution PT-OCM images in the carotid artery compared to histology; ROI 1 in Fig. 7. (a) OCM intensity image of the carotid artery. (b) H&E-stained histology of carotid artery. (c) Artery surface displacement image, excited at 1580 nm. (d) Artery surface displacement with 1720nm excitation. (e) Water compensated surface displacement image from 1720–1580 nm subtraction. (f) ORO-stained cross-section of carotid artery.

Biomedical Optics EXPRESS

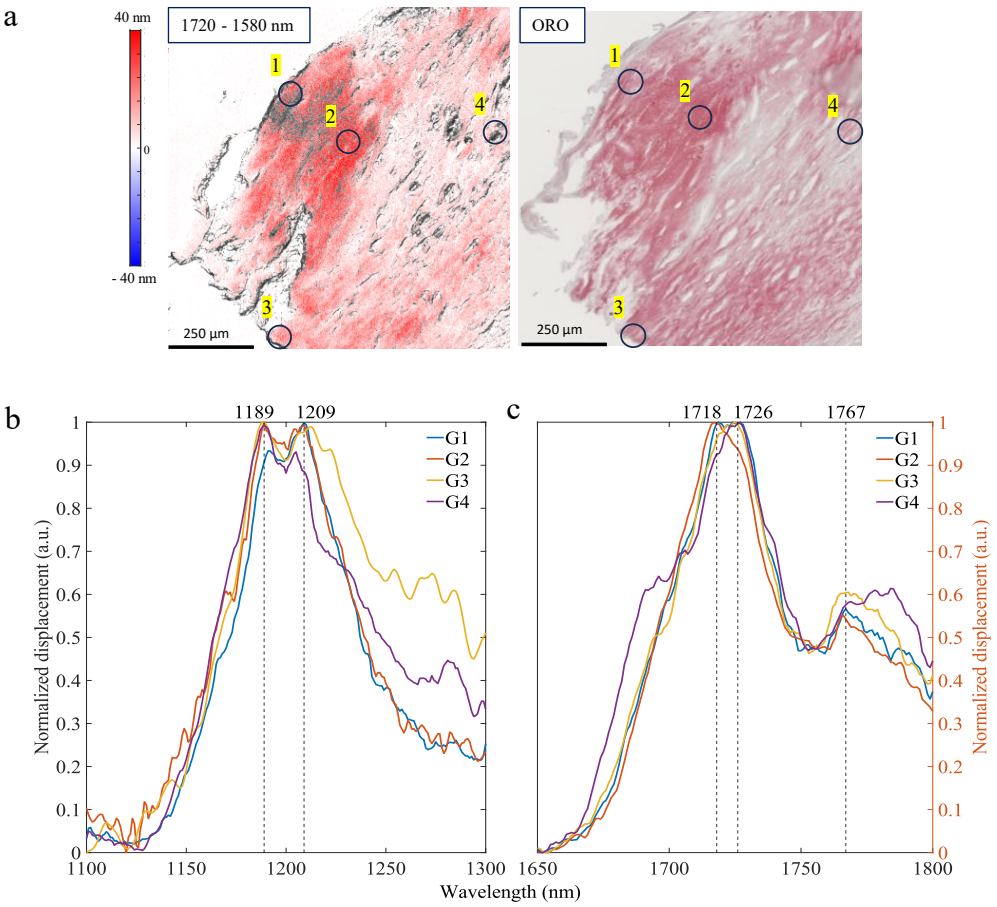

Fig. 9. PT-OCM spectra in ROI 1 (Fig. 7.) east of the vessel lumen, with group 1 closest to the lumen. (a) Water compensated surface displacement image and corresponding ORO-stained cross-section area with 4 areas highlighted for spectral analysis. (b) Spectral mean of groups 1-4 normalized across the wavelength range 1100–1300 nm (c) Spectral mean of groups 1-4 normalized across the wavelength range 1650–1800nm. G1-G4, groups 1-4.

shows a peak absorption at 1208 nm, whereas region 4's peak absorption occurs at 1190 nm. The spectra from regions 2 and 3 exhibit an equal weighting of the two distinct absorption peaks. In the wavelength range of 1650 to 1800nm, displayed in Fig. 11(c), the absorption profiles of all four regions converge around a peak at approximately 1725nm. However, the secondary absorption peak around 1769nm is less pronounced across the regions.

Biomedical Optics EXPRESS

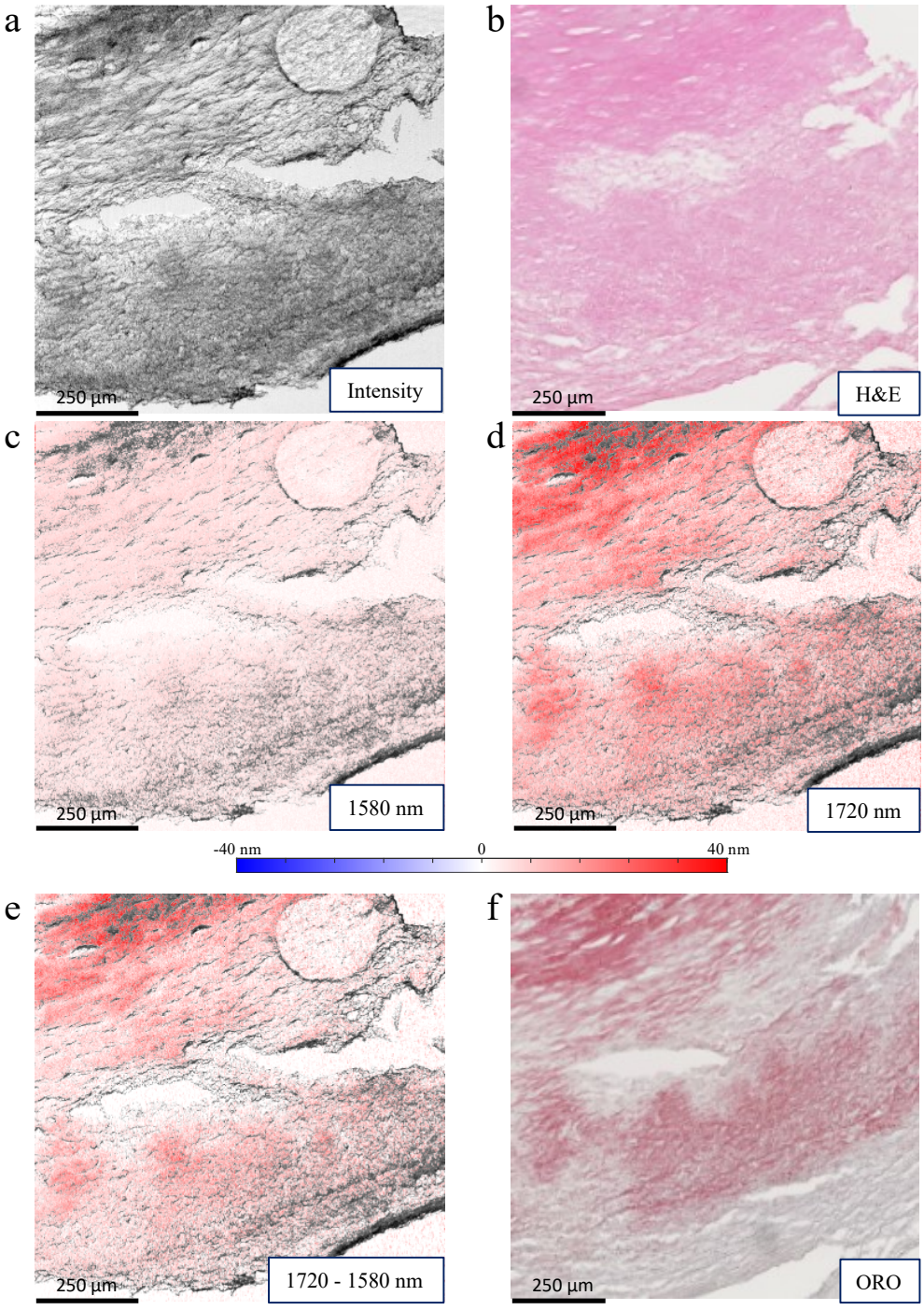

Fig. 10. High-resolution PT-OCM images of a carotid endarterectomy specimen compared to histology in ROI 2 (Fig. 7). (a) OCM intensity image of the carotid artery. (b) H&E-stained histology of carotid artery. (c) Artery surface displacement image, excited at 1580 nm. (d) Artery surface displacement with 1720nm excitation. (e) Water compensated surface displacement image from 1720–1580 nm subtraction. (f) ORO-stained cross-section of carotid artery.

Biomedical Optics EXPRESS

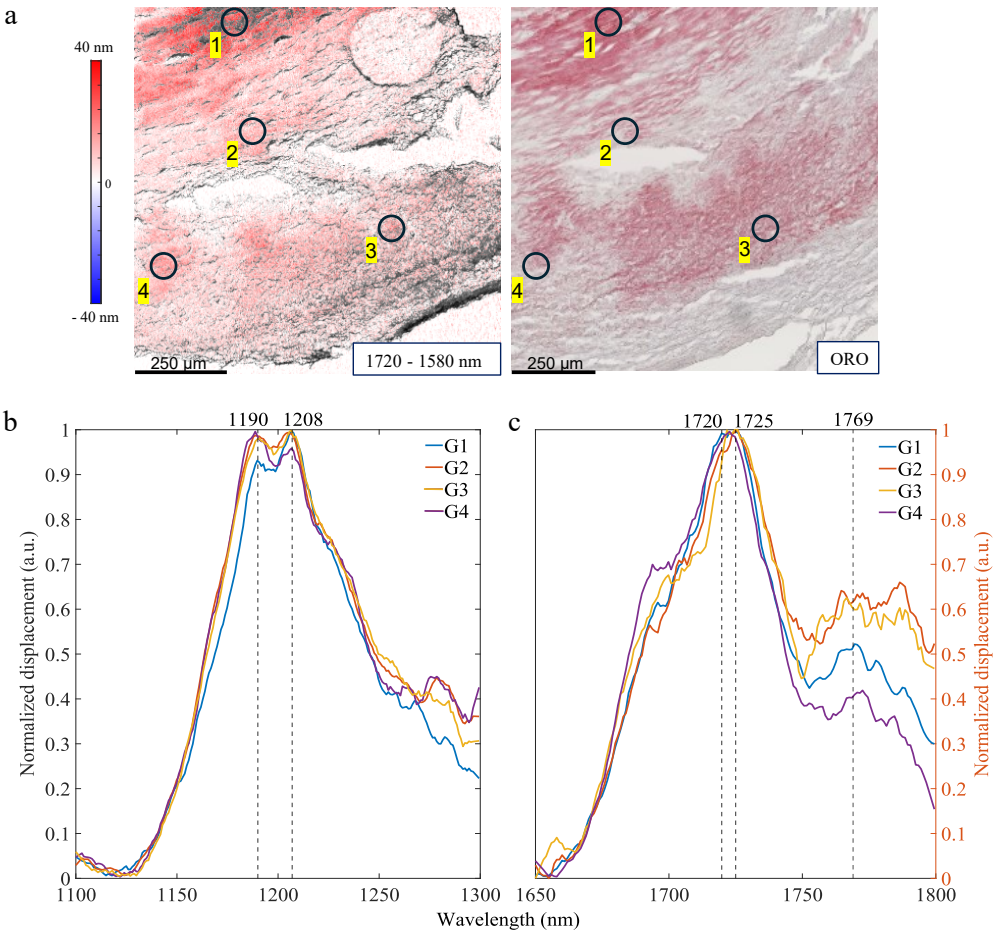

Fig. 11. PT-OCM spectra of ROI 2 (see Fig. 7.) south of the vessel lumen, with group 1 closest to the lumen. (a) Water compensated surface displacement image and corresponding ORO-stained cross-section area with 4 areas highlighted for spectral analysis. (b) Spectral mean of groups 1-4 normalized across the wavelength range 1100–1300 nm (c) Spectral mean of groups 1-4 normalized across the wavelength range 1650–1800nm. G1-G4, groups 1-4.

4. Discussion

Photothermal optical coherence microscopy (PT-OCM) offers unique advantages in optical absorption contrast imaging, by negating the need for tissue staining or contact. In this work, we increase the range of possible applications of PT-OCM to high spatial resolution spectroscopy, in which the lipid distribution in biological tissue can be determined. This is made possible by the combination of an OCT system with MHz A-line rate, a diffraction-limited spot size for surface interrogation, and a widely wavelength tunable pulsed laser. Human carotid endarterectomy samples (CEAs) were first imaged by 2D raster scanning of the entire surface area at reduced resolution, followed by high-resolution imaging of two regions of interest. Both the obtained large area sample ‘maps’ at 1720nm excitation and high-resolution small area qualitatively suggest a relation with ORO and H&E histology. Raster scanning was followed by subsequent spectroscopy at various regions of interest across two distinct lipid absorption bands. Within both absorption

Biomedical Optics EXPRESS

bands, 1100 - 1300 nm and 1650–1800nm, a notable shift in the ratio of peak absorption occurs between 1189 and 1209 nm in the first band and 1720 and 1726nm in the second.

In our previous work, we demonstrated the spectroscopic capabilities of photothermal imaging in pure lipid samples. However, when attempting translation to biologically complex samples, it was difficult to discern spectral features [36]. This was likely due to the large excitation and probe volumes in which spectra would then consist of a multitude of contributions from various tissue components.

In reported literature, PT-OCT has had limited success, particularly in its microscopic implementation. Salimi et al. acquired lipid and collagen spectra in Transient Mode PT-OCT using mayonnaise and chicken cartilage [37]. Still, as demonstrated in our previous work, the transition to human tissue is non-trivial. The initially acquired spectra of various cholesteryl esters were performed in comparison to previous work by our group, in which similar spectral features were observed [38]. More significantly, our group previously performed lipid imaging similarly in CEAs using photoacoustic spectroscopy across the 1150–1240 nm wavelength range, which was supplemented by principal component analysis decomposition and matrix-assisted laser desorption/ionization mass spectrometry imaging (MALDI-MSI). Their findings corroborate the spectral patterns demonstrated by PT-OCM in which variations in the ratio of peak absorption occur relative to the proximity of the lipid to the lumen [39].

The spectroscopic contrast between lipid areas observed in Figs. 9 and 11, relates to differences in molecular structure and confirms insights from photoacoustic (PA) imaging [40,41]. A spatially matched comparison between micro-spectroscopic PA and mass spectroscopy imaging revealed that the relative weights of the peaks in the lipid spectra are governed by the length, and the number of double bonds in the acyl chains of the various lipids but not directly to lipid class [39]. Consequently, while we successfully highlight variations in lipid distribution, we do not differentiate molecular composition.

The obvious limitation of our work for practical application lies in our low imaging speed which occurs for two reasons. First, the pulse laser was operated at 100 Hz as this resulted in a lower fluctuation in pulse energy (compared to the maximum of 200 Hz). Second, due to the use of linear motorized stages, imaging speed is limited to ensure high location repeatability. Considering the 1.6 MHz A-line acquisition rate with approximately 8 A-lines required per frame, the system can potentially achieve frame acquisition speeds up to 180 kHz, assuming proper selection of system and imaging parameters to prevent tissue heating. Such acquisition speeds coupled with galvo mirrors for scanning, could have the potential for fast imaging of tissue sections.

The ability to obtain spectroscopic information coupled with high-resolution imaging of tissue microstructure offers many opportunities. We believe that PT-OCM could potentially become a microscopic tool in pathology, offering histology-like images in a label-free form.

5. Conclusion

In this work we have demonstrated the potential of Photothermal optical coherence microscopy (PT-OCM) as a tool in optical absorption contrast imaging, without the need for tissue staining or sample contact. By integrating an OCT system with a MHz A-line rate, a diffraction-limited spot size, and a tunable pulsed laser, PT-OCM successfully extends its application to high spatial resolution spectroscopy. This method allows for detailed lipid distribution mapping in biological tissues, as evidenced by the correlation with ORO and H&E histology in carotid endarterectomy samples. The advancement in frame acquisition rates and potential real-time imaging capabilities highlight PT-OCM's promise for future clinical and research applications in lipid imaging.

Acknowledgements. The authors thank Robert Beurskens and Kim van Gaalen for their support in electronics and histology respectively.

Biomedical Optics EXPRESS

Disclosures. Gijs van Soest is a cofounder of, and has equity in, Kaminari Medical BV, who were not involved in the submitted work. In the past three years, he was the PI on research projects, administered by Erasmus MC, that received research support from FUJIFILM VisualSonics, Shenzhen Vivolight, Boston Scientific, Waters and Mindray (outside the submitted work). Ton van der Steen is a cofounder of, and has equity in, Kaminari Medical BV. The other authors declare no conflicts of interest.

Data availability. Data underlying the results presented in this paper is not publicly available at this time but may be obtained from the corresponding authors upon reasonable request.

References

1. B. E. Bouma, J. F. de Boer, D. Huang, *et al.*, "Optical coherence tomography," Nat. Rev. Methods Primers **2**(1), 79 (2022).
2. S. Aumann, S. Donner, J. Fischer, *et al.*, "Optical Coherence Tomography (OCT): Principle and Technical Realization," *High Resolution Imaging in Microscopy and Ophthalmology* (Springer International Publishing, 2019), pp. 59–85.
3. A. D. Aguirre and J. G. Fujimoto, "Optical Coherence Microscopy," in *Optical Coherence Tomography* (Springer International Publishing, 2008), pp. 505–542.
4. P. Tankam, Z. He, G. Thuret, *et al.*, "Capabilities of Gabor-domain optical coherence microscopy for the assessment of corneal disease," J. Biomed. Opt. **24**(4), 046002 (2019).
5. K. Grieve, O. Thouvenin, A. Sengupta, *et al.*, "Appearance of the retina with full-field optical coherence tomography," Invest. Ophthalmol. Vis. Sci. **57**(9), OCT96–OCT104 (2016).
6. I. K. Jang, G. J. Tearney, B. MacNeill, *et al.*, "In vivo characterization of coronary atherosclerotic plaque by use of optical coherence tomography," Circulation **111**(12), 1551–1555 (2005).
7. M. Araki, S. J. Park, H. L. Dauerman, *et al.*, "Optical coherence tomography in coronary atherosclerosis assessment and intervention," Nat. Rev. Cardiol. **19**(10), 684–703 (2022).
8. R. F. Spaide, J. G. Fujimoto, N. K. Waheed, *et al.*, "Optical coherence tomography angiography," Prog. Retin Eye Res. **64**, 1–55 (2018).
9. Y. Li, J. Jing, E. Heidari, *et al.*, "Intravascular Optical Coherence Tomography for Characterization of Atherosclerosis with a 1.7 Micron Swept-Source Laser," Sci. Rep. **7**(1), 1–6 (2017).
10. V. Kuttippurath, N. Slijkhuis, S. Liu, *et al.*, "Spectroscopic optical coherence tomography at 1200 nm for lipid detection," J. Biomed. Opt. **28**(09), 1–12 (2023).
11. A. L. Oldenburg, C. Xu, and S. A. Boppart, "Spectroscopic optical coherence tomography and microscopy," IEEE J. Select. Topics Quantum Electron. **13**(6), 1629–1640 (2007).
12. A. Lichtenegger, D. J. Harper, M. Augustin, *et al.*, "Spectroscopic imaging with spectral domain visible light optical coherence microscopy in Alzheimer's disease brain samples," Biomed. Opt. Express **8**(9), 4007 (2017).
13. U. Morgner, W. Drexler, X. Li, *et al.*, "Spectroscopic optical coherence tomography," Opt. Lett. **25**(2), 111–113 (2000).
14. H. S. Nam and H. Yoo, "Spectroscopic optical coherence tomography: A review of concepts and biomedical applications," Appl Spectrosc Rev. **53**(2-4), 91–111 (2018).
15. Y. Li, S. Moon, J. J. Chen, *et al.*, "Ultrahigh-sensitive optical coherence elastography," Light: Sci. Appl. **9**(1), 58 (2020).
16. M. Singh, F. Zvietcovich, F. Zvietcovich, *et al.*, "Introduction to optical coherence elastography: tutorial," J. Opt. Soc. Am. A **39**(3), 418–430 (2022).
17. K. V. Larin and D. D. Sampson, "Optical coherence elastography – OCT at work in tissue biomechanics [Invited]," Biomed. Opt. Express **8**(2), 1172 (2017).
18. Z. Chen, G. Liu, B. J. Tromberg, *et al.*, "A comparison of Doppler optical coherence tomography methods," Biomed. Opt. Express **3**(10), 2669–2680 (2012).
19. R. A. Leitgeb, R. M. Werkmeister, C. Blatter, *et al.*, "Doppler Optical Coherence Tomography," Prog. Retin. Eye Res. **41**, 26–43 (2014).
20. B. Braaf, M. G. O. Gräfe, N. Uribe-Patarroyo, *et al.*, "OCT-Based Velocimetry for Blood Flow Quantification," in *High Resolution Imaging in Microscopy and Ophthalmology*, (Springer International Publishing, 2019), pp. 161–179.
21. J. F. de Boer, C. K. Hitzenberger, and Y. Yasuno, "Polarization sensitive optical coherence tomography – a review [Invited]," Biomed. Opt. Express **8**(3), 1838 (2017).
22. B. Baumann, A. Woehrer, G. Ricken, *et al.*, "Visualization of neuritic plaques in Alzheimer's disease by polarization-sensitive optical coherence microscopy," Sci. Rep. **7**(1), 43477 (2017).
23. P. Tang and R. K. Wang, "Polarization sensitive optical coherence tomography for imaging microvascular information within living tissue without polarization-induced artifacts," Biomed. Opt. Express **11**(11), 6379–6388 (2020).
24. D. C. Adler, S.-W. Huang, R. Huber, *et al.*, "Photothermal detection of gold nanoparticles using phase-sensitive optical coherence tomography," Opt. Express **16**(7), 4376–4393 (2008).
25. C. Pache, A. Bouwens, N. L. Bocchio, *et al.*, "Fast three-dimensional imaging of gold nanoparticles in living cells with photothermal optical lock-in Optical Coherence Microscopy," Opt. Express **20**(19), 21385–21399 (2012).
26. M. C. Skala, M. J. Crow, A. Wax, *et al.*, "Three-dimensional molecular imaging with photothermal optical coherence tomography," Methods Molecular Biol. **1026**, 85–92 (2013).
27. J. H. Pai, T. Liu, H. Y. Hsu, *et al.*, "Molecular photo-thermal optical coherence phase microscopy using gold nanorods," RSC Adv. **4**(51), 27067–27073 (2014).

Biomedical Optics EXPRESS

28. J. Sun, H. Wang, T. Fang, *et al.*, "Photothermal optical coherence tomography for 3D live cell detection and mapping," Opt. Continuum **2**(12), 2468–2483 (2023).
29. M. H. Salimi, M. Villiger, M. Villiger, *et al.*, "Transient-mode photothermal optical coherence tomography," Opt. Lett. **46**(22), 5703–5706 (2021).
30. J. Wu, N. Wu, P. Tang, *et al.*, "Pulse photothermal optical coherence tomography for multimodal hemodynamic imaging," Opt. Lett. **46**(22), 5635 (2021).
31. A. Doug Deen, H. M. M. Van Beusekom, T. Pfeiffer, *et al.*, "Spectroscopic thermo-elastic optical coherence tomography for tissue characterization," Biomed. Opt. Express **13**(3), 1430 (2022).
32. S. Karpf, T. Klein, T. Pfeiffer, *et al.*, "High definition live 3D-OCT in vivo: design and evaluation of a 4D OCT engine with 1 GVoxel/s," Biomed. Opt. Express **5**(9), 2963–2977 (2014).
33. "Thorlabs - R3L3S1N Negative 1951 USAF Test Target, 3" x 3"," https://www.thorlabs.com/thorproduct.cfm?partnumber=R3L3S1N.
34. C. P. Fleming, J. Eckert, E. F. Halpern, *et al.*, "Depth resolved detection of lipid using spectroscopic optical coherence tomography," Biomed. Opt. Express **4**(8), 1269 (2013).
35. P. Wang, H. W. Wang, M. Sturek, *et al.*, "Bond-selective imaging of deep tissue through the optical window between 1600 and 1850nm," J. Biophotonics **5**(1), 25–32 (2012).
36. A. Doug Deen, T. Pfeiffer, H. M. M. van Beusekom, *et al.*, "Thermo-elastic optical coherence microscopy," in *Advanced Chemical Microscopy for Life Science and Translational Medicine*, G. J. Simpson, J.-X. Cheng, and W. Min, eds. (SPIE, 2020), 11252, p. 15.
37. M. H. Salimi, M. Villiger, and N. Tabatabaei, "Detection of lipid at video rate with spectroscopic transient-mode photo-thermal optical coherence tomography (TM-PT-OCT)," Proc. SPIE **11948**, 119480C (2022).
38. K. Jansen, M. Wu, A. F. W. Van der Steen, *et al.*, "Photoacoustic imaging of human coronary atherosclerosis in two spectral bands," Photoacoustics **2**(1), 12–20 (2014).
39. S. Iskander-Rizk, M. Visscher, A. M. Moerman, *et al.*, "Micro Spectroscopic Photoacoustic (μsPA) imaging of advanced carotid atherosclerosis," Photoacoustics **22**, 100261 (2021).
40. K. Jansen, A. F. van der Steen, M. Wu, *et al.*, "Spectroscopic intravascular photoacoustic imaging of lipids in atherosclerosis," J. Biomed. Opt. **19**(2), 026006 (2014).
41. J. J. M. Riksen, S. Chandramoorthi, A. F. W. Van der Steen, *et al.*, "Near-infrared multispectral photoacoustic analysis of lipids and intraplaque hemorrhage in human carotid artery atherosclerosis," Photoacoustics **38**, 100636 (2024).